Chapter 3

Electrochemical performance of Delafossite, $AgFeO_2$: A Pseudocapacitive Electrode in Neutral Aqueous Na_2SO_4 Electrolyte

In this chapter, Layered delafossite $AgFeO_2$ with an open channel structure is envisaged as a pseudocapacitor electrode using Fe^{2+}/Fe^{3+} redox couple. A simple co-precipitation method was employed for the phase formation of delafossite $AgFeO_2$ resulting in a mixture of 2H and 3R-phase. 2H $AgFeO_2$ was aimed to synthesize as a majority phase because it has larger inter-layer spacing than the 3R phase. Flower-like microarchitectures of $AgFeO_2$ show outstanding electrochemical performance with a high specific capacitance of 110.4 F g^{-1} at 1 A g^{-1} current density in 1 M Na_2SO_4 electrolyte. In an asymmetric device mode, AFO-400//AC full cell exhibits superior electrochemical performance by delivering high energy density (33.5 Wh kg^{-1}) and high-power density (454.3 W kg^{-1}) with excellent cycling stability (86% retention after 2000^{th} cycles). The results clearly demonstrate that the synthesized delafossite $AgFeO_2$, having a mixture of 2H and 3R-phases has the remarkable potential to be used as a negative electrode material for supercapacitor and other energy storage technologies.

3.1 Introduction

Transition metal oxides and hydroxides exhibit multiple oxidation states and possess unique crystal structures that enable fast faradic redox/intercalation reactions at their interfaces, leading to superior performance as pseudocapacitive electrodes. Commonly used materials for pseudocapacitor electrodes include RuO_2, MnO_2, V_2O_5, NiO, and Co_3O_4, as well as their mixtures, such as $NiCo_2O_4$ and V_2O_5/MnO_2 core-shell nanotubes. Theoretical capacitance values for RuO_2, MnO_2, V_2O_5, NiO, and Co_3O_4 in aqueous electrolytes are 2200, 1370, 2120, 2584, and 3560 F g^{-1}, respectively. However, the theoretical capacitances of these metal oxides have rarely been achieved in experiments due to their poor electronic conductivity, which limits their rate performance under high-power applications. Numerous efforts have been made to enhance the electrochemical performance of these metal oxides by modifying their structure, and compositions, or incorporating other metals into their frameworks. Recent literature has demonstrated the development of hybrid devices that combine a capacitive electrical double-layer (EDL) electrode with a battery-type electrode, aiming to achieve high power and energy simultaneously within a single component.

Most of the transition metal oxides showed superior performance in positive windows. In search of negative electrodes, iron oxides/hydroxides are getting tremendous interest, because of their significant merits such as: (1) iron possesses multiple valence states (Fe^0, Fe^{2+}, Fe^{3+}, Fe^{4+}, etc.) and rich redox chemistry (Fe^0/Fe^{2+}, Fe^0/Fe^{3+}, Fe^{2+}/Fe^{3+}, Fe^{3+}/Fe^{4+}, etc.), enabling them high specific capacity [162]–[164]; (2) iron oxides/hydroxides are less toxic and more environ-friendly than other transition metal oxides/hydroxides [165]; (3) iron oxides/hydroxides are earth-abundant (iron is the richest transition metal element in the Earth's crust) and inexpensive, which are suitable for commercial applications[166]. It is well known that the morphology, composition, and crystal structure of iron-based materials have significant influences on their electrochemical performance. However, the current iron-based electrodes for supercapacitors face a major obstacle due to their poor electrochemical and cycling performance. To address this issue, several effective strategies have been implemented to overcome these limitations of iron-based materials, these include nanostructural design [167], foreign ion doping to make solid solution [36], and the introduction of oxygen vacancies into the lattices [168].

In this work, a silver-iron-containing binary metal oxide in a single crystal structure was selected and investigated as a negative electrode for pseudocapacitance. The equimolar ratio of silver and iron crystallizes into delafossites-type minerals having a layered structure of formula ABO_2, where A typically represents monovalent cation (e.g., Ag^+, Cu^+, Pt^+, etc.) that arranges orthogonally with edge-sharing BO_6 octahedra (with B = Fe^{3+}, Ni^{3+} or other trivalent metal cations) along the c-axis. Depending on the orientation of each layer along the c-axis, $AgFeO_2$ can adopt two different polytypes: 3R (rhombohedral) and 2H (hexagonal). A pure 3R-$AgFeO_2$ and 2H-$AgFeO_2$ can be prepared separately under specific conditions of high pressure of 3 and 6 GPa, as developed by Terada et al. To date, very few reports exist about delafossites-type minerals as alternative electrodes for supercapacitors (e.g., $CuCrO_2$ [169], $CuMnO_2$ [170], $CuNiO_2$ [171] and its composites), while none of these use silver-iron based compounds, to the best of our knowledge.

A simple co-precipitation method was employed for the phase formation of delafossite $AgFeO_2$, resulting in a mixture of 2H and 3R phases. The electrochemical properties of $AgFeO_2$ calcined at 400 °C, predominantly composed of the 2H phase, exhibited excellent performance in terms of energy storage and cyclic stability. Additionally, in an asymmetric device configuration, where AFO-400 served as the negative electrode and activated carbon as the positive electrode in 1M Na_2SO_4 electrolyte, demonstrated superior electrochemical performance compared to other recently reported iron-based materials. This superiority was confirmed through cyclic voltammetry, charge/discharge, and electrochemical impedance spectroscopy techniques.

3.2 Experimental

3.2.1 Preparation of active martials

$AgFeO_2$ nanoparticles were prepared by a modified co-precipitation route. Typically, 5 mM of silver nitrate ($AgNO_3$, 99.9%, HIMEDIA) and 5 mM of iron nitrate ($Fe(NO_3)_3.9H_2O$, 98%, Merk) were dissolved in 200 ml of double distilled water with continuous stirring to make a homogeneous solution. Further, 50 ml of 5 M NaOH solution acting as precipitating agent, was added dropwise in the above solution and the pH of the mixture was adjusted to 10 by the complete addition of 5 ml, 25% ammonia solution. The suspension was allowed to stand for 6 h for complete precipitation followed by washing

repeatedly with doubled distilled water and ethanol. The filtrate was collected and dried at 80 °C for 12 h in a vacuum oven and calcined at 200, 400, and 550 °C for 5 h in an air atmosphere. The samples are abbreviated as AFO-80 (not calcined), AFO-200, AFO-400, and AFO-550 respectively in the rest of this chapter. All synthesized powder samples were deep brown in color and further used for structural and other analyses without any pre-conditioning.

3.2.2 Material characterizations

The crystallinity and phase identification of the synthesized materials were confirmed by room temperature X-ray diffraction (XRD) using Cu-Kα radiation (λ = 1.54 Å) operated at 40 kV and 15 mA between 2θ of 10°−80° at a scan rate of 3° per minute in Bragg-Brentano configuration. The thermal stability of materials was investigated by thermogravimetry (TG) and differential thermal analysis (DTA) using a simultaneous TG-DTA Thermal analyzer (Mettler Toledo, Germany) in the temperature range of 25 °C–850 °C with a constant heating rate of 10 °C per minute in N_2 atmosphere. The structural analysis of materials was confirmed by Raman and Fourier Transform Infrared (FTIR) spectroscopy. Raman spectroscopy was carried out at room temperature using Renishaw inVia Raman microscope in the wavenumber range of 150 to 800 cm^{-1}. An argon ion laser having a power of 10 mW and wavelength (532 nm) was used as an excitation source. The laser beam was focused on the surface of the sample by applying a constant laser power with an acquisition time of 10 s to enhance the S/N ratio. FTIR spectra of all samples such as AFO-80, AFO-200, AFO-400, and AFO-550 were taken in the range of 400–2500 cm^{-1} using a Perkin Elmer FTIR spectrometer. The specimens were pressed into small, thin pellets using a pure KBr. The microstructure of synthesized materials was examined by a High-Resolution Scanning Electron Microscope (HR-SEM) of Nova Nano SEM-450 equipped with an EDS system. The lattice spacing of AFO-400 nanoparticles was obtained by using FEI TecnaiF30 HRTEM operated at 300 kV.

3.2.3 Preparation of electrode for electrochemical measurements

Electrochemical measurements were performed with the help of an electrochemical workstation Metrohm Autolab (PGSTAT204) equipped with an FRA32M module. A three-electrode setup consisting of active material coated carbon paper of square area 1 cm^2 as a

working electrode, Hg/HgO/20% KOH as a reference electrode, and a platinum wire as a counter electrode, respectively, was used. The working electrode was prepared by mixing synthesized active material (70%) conducting activated carbon (20%) and polyvinylidene difluoride (PVDF) (10%) as a binder in N-methyl pyrrolidone (NMP), which was used as a solvent. The prepared mixture was drop cast on carbon paper (1 × 1 cm^2) and dried at 80 °C for 12 h in a vacuum oven. The mass of the active material loaded on the substrate was approximately 1 mg. The asymmetric cell was fabricated by sandwiching AFO-400 and activated carbon electrode deposited on a 1 × 1 cm^2 area of Torey carbon paper, with a cellulose separator soaked in 1 M Na_2SO_4 electrolyte. Electrochemical analysis was done with the help of NOVA 1.11 software by performing cyclic voltammetry, galvanostatic charge/discharge, and electrochemical impedance spectroscopy in 1 M Na_2SO_4 electrolyte.

3.3 Results and Discussion

3.3.1 X-ray study

The crystallinity and phase identification/purity of differently made delafossites such as AFO-80, AFO-200, AFO-400, and AFO-550 were characterized by powder X-ray diffraction method and XRD pattern are displayed in Fig. 3.1. The X-ray diffraction patterns recorded in the 2θ range of 10°−80°, show both sharp and broader diffraction peaks and identified as two polytypes; one is 2H (JCPDS no. 75-2147) and other one is 3R (JCPDS no. 25-0765) phase of $AgFeO_2$. Mixed-phase polytypes are usually formed during the process of low-temperature synthesis of delafossites [172]. All diffraction peaks are indexed and matched with $AgFeO_2$. No impurity peaks corresponding to metallic silver, Ag_2O, and FeOOH could be detected in the XRD pattern. The interlayer spacing of (00l) is almost equal in both the 2H and 3R phases which makes it very difficult to find out the individual phase contribution of each phase in the materials. However, a broader asymmetric peak is observed in the range 45°−58°, which is a combination of both (108) of 2H (green solid line) and (105) of 3R phase (blue solid line). This broader peak was resolved/deconvoluted into two peaks to get the individual phase fraction analysis of each phase in the material. Fig. 3.2 shows the deconvolution of the selected broad peak. It was noticed that as the temperature increases from 80 °C to 400 °C, the concentration of the 2H phase increases from 32% to 62% and the 3R phase decreases from 67% to 37%. Thus, the 2H phase grows at the expense of the 3R

phase by raising the calcination temperature demonstrated in Table 3.1. Further increasing the temperature to 550 ° C, the $AgFeO_2$ starts decomposing to Ag^0 and Fe_2O_3 [as depicted in Fig. 3.1 (magenta solid line)].

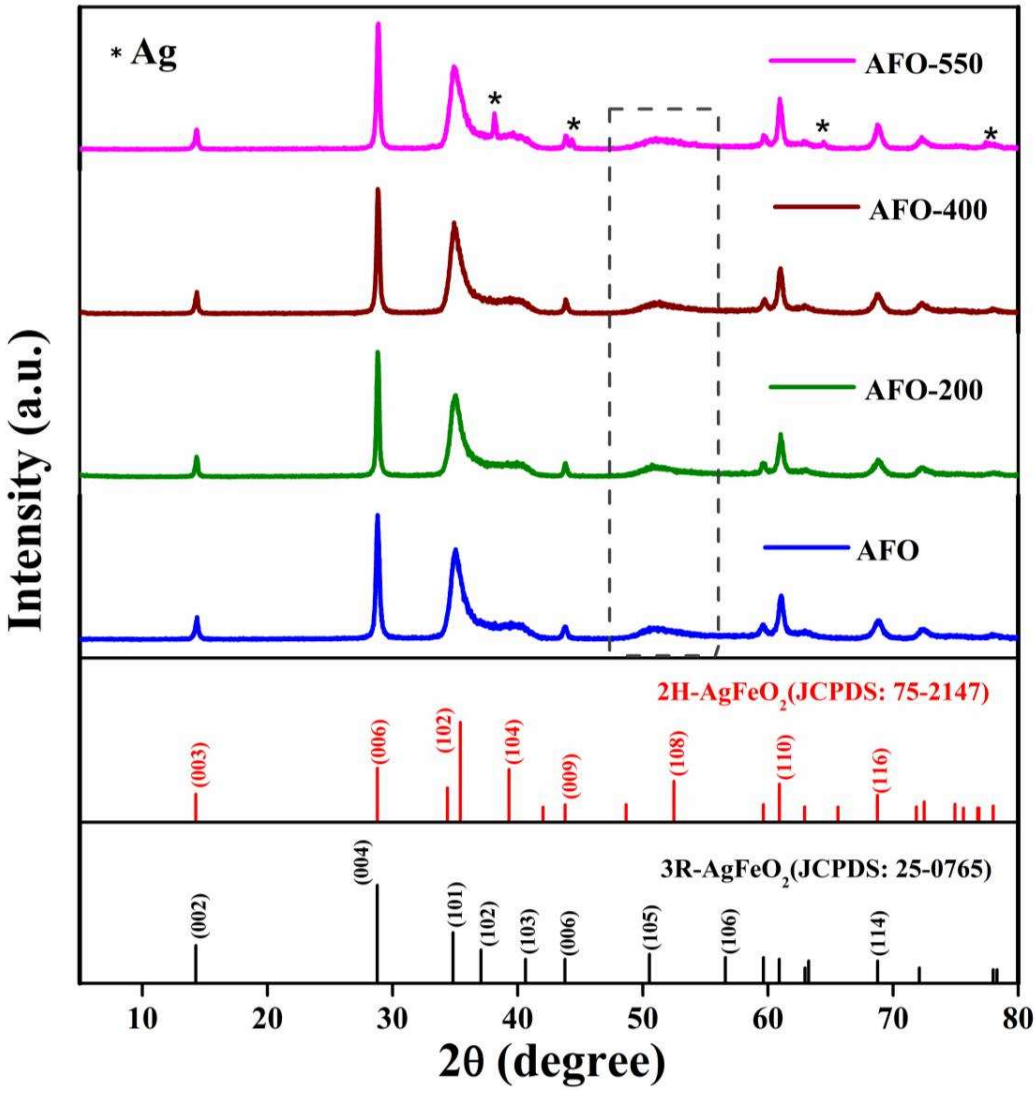

Figure 3.1: XRD pattern of different electrodes AFO-80, AFO-200, AFO-400, and AFO-550 along with their 2H and 3R JCPDS pattern file.

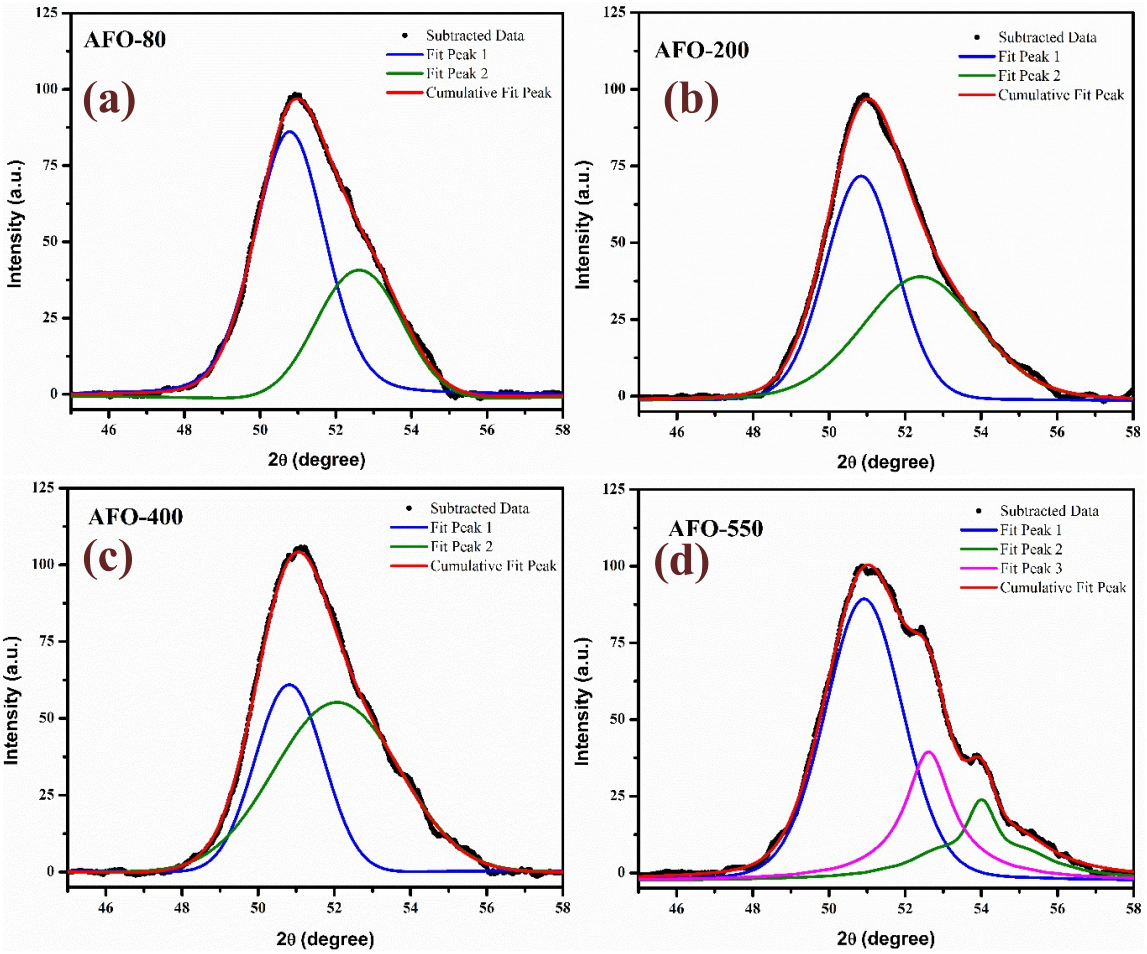

Figure 3.2: Deconvolution of XRD data into two peaks one at 50.52 for the 3R phase (blue solid line) and another at 52.5 for the 2H phase (green solid line) in (a) to (c) whereas in (d) one additional peak at 51.7 correspond to Ag^0 (magenta solid line).

Table 3.1: Represents the A_1 area under the curve of the (105) plane and A_2 of the (108) plane along with fitting parameters of various electrodes synthesized at different temperatures.

Sample	A_1	A_2	A_3	X^2	R^2
AFO-80	67.16764	32.46456		1.195	0.998
AFO-200	52.3383	47.6616		1.387	0.998
AFO-400	36.916	61.9784		1.308	0.998
AFO-550	A_1	A_2	A_3	1.076	0.999
	59.9018	16.71993	23.37819		

3.3.2 Morphological analysis

The morphology and particle size distribution of AFO-80 and AFO-400 are determined from scanning electron micrographs. The SEM image of AFO-80 indicates inhomogeneous agglomerated particles, whose size roughly spans from 20 to 100 nm shown in Fig. 3.3(a). On increasing calcination temperature, particles started to segregate as AFO-400 demonstrates homogeneous particle size distribution with a mean diameter of 100 nm Fig. 3.3(b). These homogeneously distributed, highly dense spherical particles are interconnected to each other forming a 3D network and may affect the electron transportation and ion diffusion during electrochemical reactions. Figure 3.3(c) shows the SEM image of the tested AFO-400 electrode, which confirms there is no change in morphology and composition due to the electrochemical cycling. Further energy dispersive spectra, shown in Figs. 3.3(d)–3.3(f) confirm only the presence of elements Ag, Fe, and O in the sample. EDS analysis of AFO-400 given in Table 3.2 suggests $AgFeO_2$ contains the vacancy of ~0.2 Ag^+ ions in the lattice that can be reversibly exchanged by Na^+ ions during electrochemical cycling. The pseudocapacitive nature of the $AgFeO_2$ electrode can be governed by the following reaction:

$$Ag_{0.8}Fe^{+3}O_2 + 0.1Na_2SO_4 \rightleftarrows Na_{0.2}Ag_{0.8}Fe^{+3}O_2\,[SO_4^{2-}]_{0.1} \ldots\ldots EDLC - type$$

$$Ag_{0.8}Fe^{+3}O_2 + 0.2Na^+ \rightleftarrows Na_{0.2}Ag_{0.8}Fe_{0.8}^{+3}Fe_{0.2}^{+2}O_2 \ldots\ldots Pseudocapacitive - type$$

Table 3.2: Represents the EDS analysis data of AFO-80, fresh AFO-400, and electrochemically tested AFO-400.

EDS analysis of different AFO samples			
Composition	**% Ag**	**% Fe**	**% O**
AFO-80	21.87	29.42	48.71
AFO-400 fresh	22.33	28.24	49.43
AFO-400 used	22.57	29.64	47.79

A combination of EDLC and faradaic-type capacitance was observed for $AgFeO_2$ and electrochemical results will represent the detailed description of the capacitive behavior of

the material later. Theoretically for 0.2 Na^+ ions incorporation, specific capacity can be calculated using the following equation:

$$C\left(\frac{F}{g}\right) = \frac{nF}{Mol.wt.} \ldots\ldots (3.1)$$

$$C\left(\frac{F}{g}\right) = \frac{0.2 * 96485.33}{195.7120} = 98.6\ F/g$$

Which is approximately equal to the capacity obtained at a scan rate of 10 mV s^{-1}.

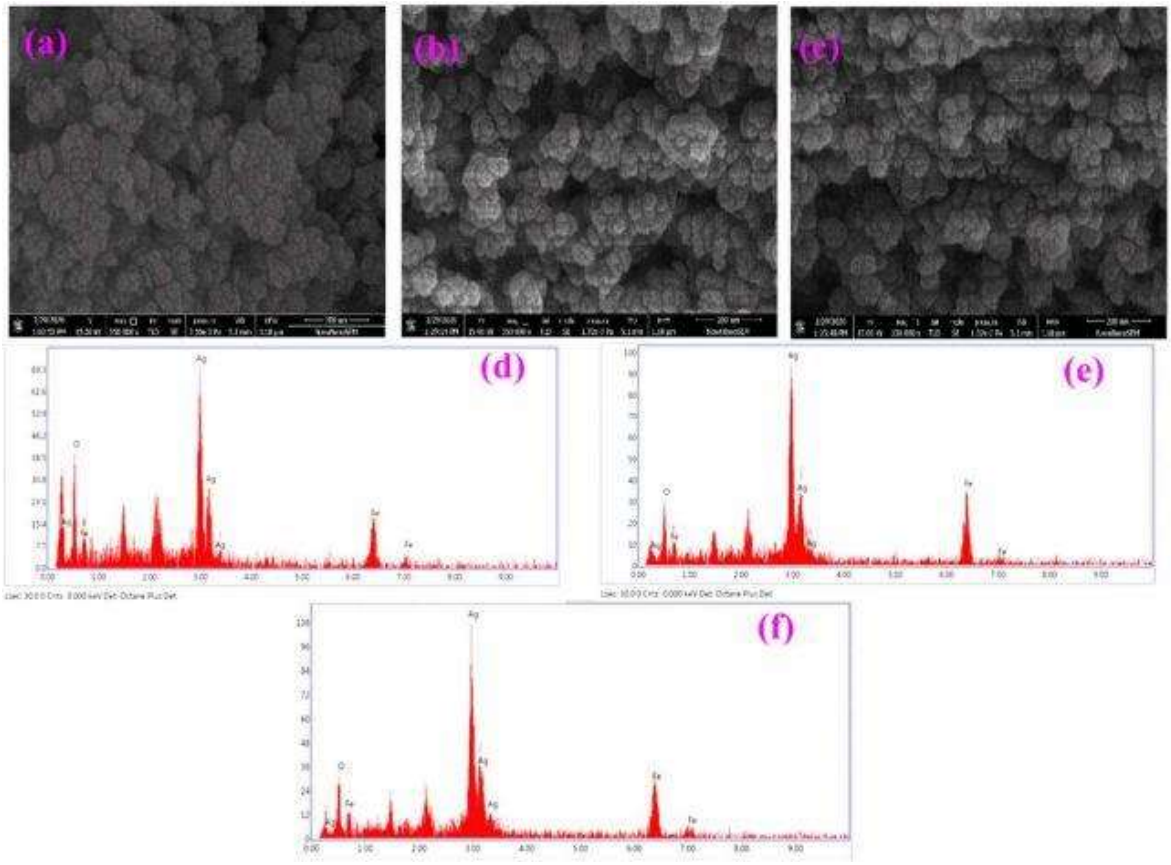

Figure 3.3: SEM images of the as-obtained samples viz. (a) AFO-80, (b) AFO-400 (fresh) (c) AFO-400 (tested) along with their corresponding EDS images shown in fig. (d), (e), and (f), respectively.

Figures 3.4a & 3.4b show the HRTEM image of the 2H and 3R phase of AFO-400, inset shows lattice fringes visible in inverse Fast Fourier transform (FFT) with their corresponding line profile. The lattice spacing of the (004) plane of the 2H phase (0.307 nm) is greater than the (012) plane of the 3R phase (0.225 nm), which is in accordance with the earlier reported co-precipitation synthesis of $AgFeO_2$ [173]. The above results confirm the coexistence of 2H and 3R phases in AFO-400 material.

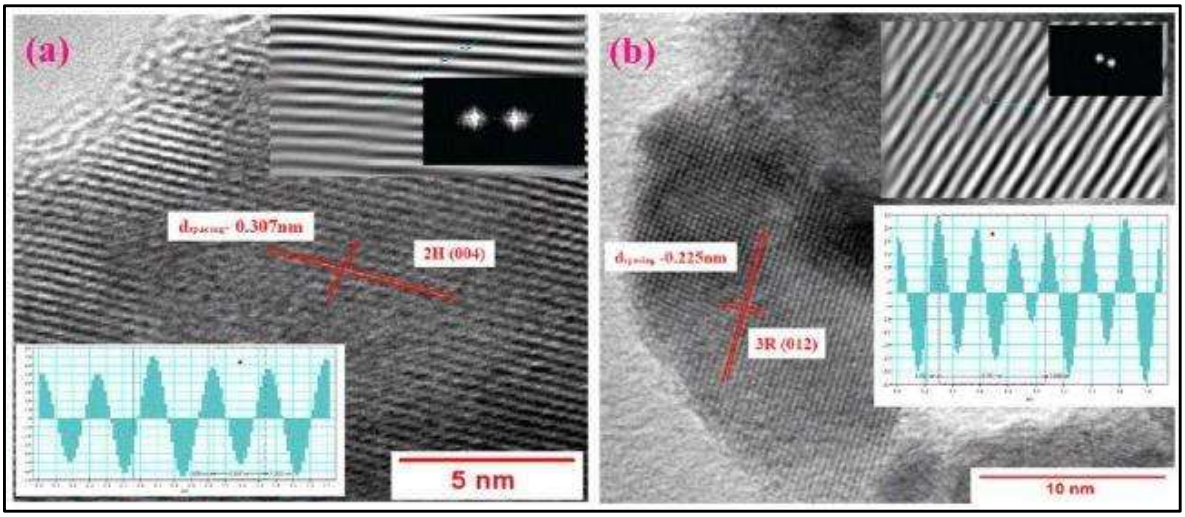

Figure 3.4: HRTEM image of 2H (a) and 3R (b) phase of AFO-400 with a lattice spacing of superstructure (inset: inverse FFT of the selected region with their Line profile).

3.3.3 Thermal analysis

In order to investigate the thermal stability of $AgFeO_2$, the TGA-DTA measurements of AFO-80 are carried out in the N_2 atmosphere in the temperature range of 25 °C to 850 °C shown in Figure 3.5. From the TGA-DTA profile, we observe mass loss with increasing temperature. For instance, while an initial 1.8% mass loss occurs which is due to the evaporation of physisorbed water, 5.3% loss of mass in the range of 100 °C–400 °C is due to the removal of hydroxyl and nitrate ions. In the temperature range of 375 °C–400 °C, the flat nature of the TGA profile indicates the stability of the phase. Further, 1.9% of loss in the range of 400 °C–600 °C is due to the slow removal of Ag from $AgFeO_2$ as evident with an extra peak of Ag observed in the pXRD of AFO-550 [Fig. 3.1]. An additional 3.7% of loss above 600 °C is observed due to the complete decomposition of $AgFeO_2$ to Ag and Fe_2O_3.

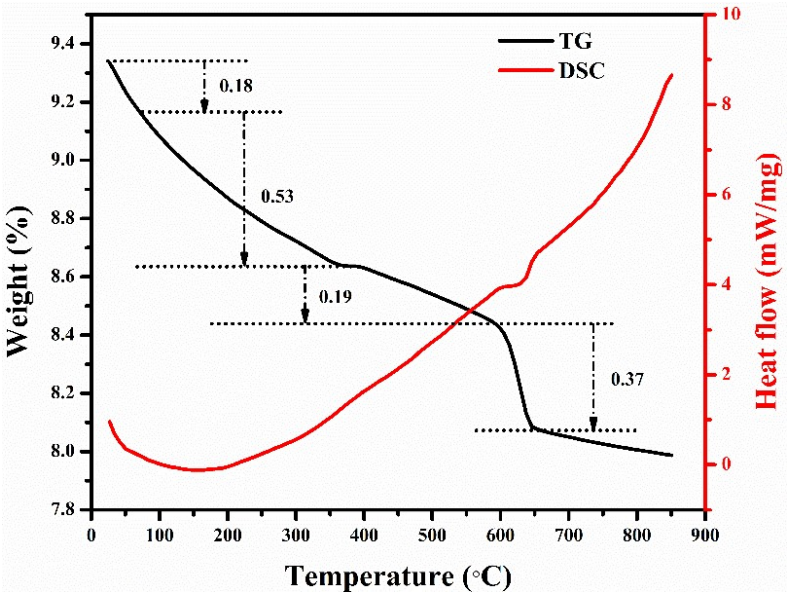

Figure 3.5: Thermogravimetric analysis (TGA) and differential thermal analysis (DTA) profile of AFO-80 under N_2 atmosphere.

3.3.4 Raman and FT-IR analysis

Raman spectra of synthesized samples are shown in Fig. 3.6(a). The point group associated with the 3R phase is C_{3v}, with one molecular unit in its primitive cell and its corresponding Raman vibration modes are described by following reducible representation:

$$\Gamma = 1A_{1g} + 3A_{2u} + 1E_g + 3E_u$$

The A, symmetry represents the vibration of the Ag–O bond along the c-axis whereas the E symmetry corresponds to the vibration of the triangular lattice of FeO_6 octahedra perpendicular to the c-axis. The delafossite-type structure has an inversion center, which leads to an even and odd vibrational mode. The even modes (A_{1g} and E_g) are Raman active while odd modes (A_{2u} and E_u) are found to be an acoustic phonon vibration active in the IR region. On the other hand, the 2H phase has a D_{6h} point group with two molecular units in its primitive cell and possesses more Raman active modes than its 3R counterpart. The following Raman active vibrations are described by reducible representations:

$$\Gamma = 1A_{1g} + 3A_{2u} + 1E_g + 3E_u$$

According to Raman analysis, two broad peaks at 383 cm^{-1} and 584 cm^{-1} are observed, which correspond to E_g and A_{1g} vibration modes respectively. The E_g mode is associated with Fe–O–Fe bending, while the A_{1g} mode is related to Ag–O stretching along the c-axis. A broad peak around 500 cm^{-1} is attributed to the surface plasmon resonance of the material mixture. The aforementioned features do not change with increasing calcination temperature.

FTIR spectroscopy has been used to solidify the previous observations and to obtain a clear picture of synthesized silver ferrites. Fig. 3.6(b) represents the FTIR spectra of various silver ferrites in the range of 400–2500 cm^{-1}. The IR spectra show the strongest bands at 472 and 613 cm^{-1} which corresponds to the bending vibration of Fe^{3+} ions located in FeO_6 octahedral units and Ag^{+} ions in linear O–Ag–O coordination respectively. The second most intense absorption band located at 1380 cm^{-1} along with a faint band around 890 cm^{-1} is in accordance with the stretching and bending vibrational modes of Fe–O–H in α-FeOOH. The remaining weak bands in the spectrum of $AgFeO_2$ are due to slight impurities of nitrate and OH^{-} ions, whereas the other features can be associated with vibration modes of the 2H structure. With increasing calcination temperature, the drop in the intensity of the above bands is observed which indicates the removal of adsorbed impurities from the material.

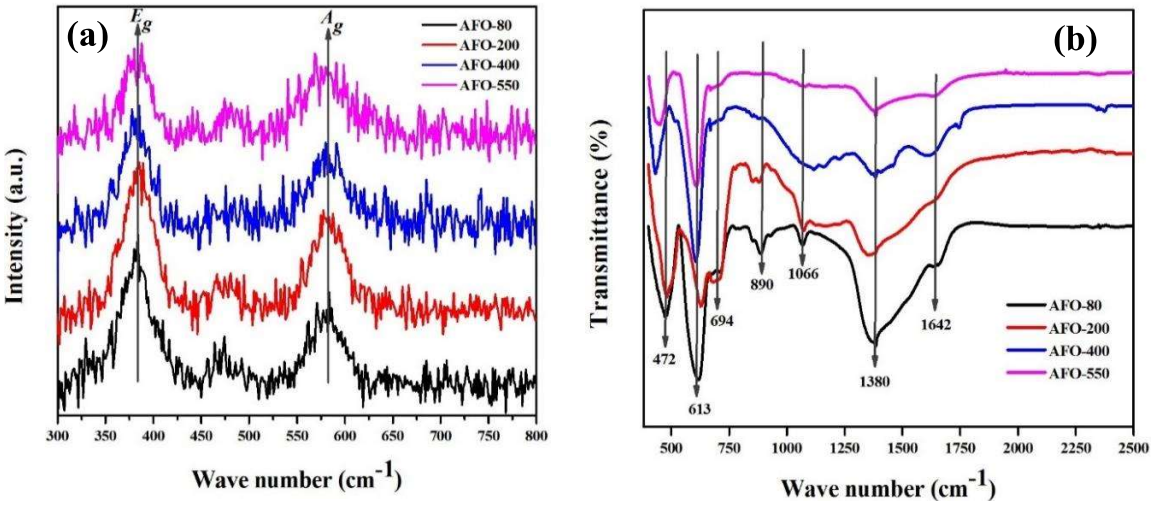

Figure 3.6: Raman (a) and FTIR (b) spectra of different electrodes viz. AFO-80, AFO-200, AFO-400, and AFO-550

3.3.5 Electrochemical analysis

Cyclic voltammetry (CV) and galvanostatic charge/discharge (GCD) measurements are initially performed to elucidate the electrochemical performance of the as-prepared electrodes using a three-electrode setup in 1 M Na_2SO_4 electrolyte. Fig. 3.7a represents an overlay of CV curves obtained for AFO-80, AFO-200, AFO-400, and AFO-550 at a scan rate of 10 mV s^{-1} within potential window 0.1 to −0.9 V. All electrodes display a pair of reversible peaks, suggesting a pseudo capacitive nature of electrodes that results from redox couple of Fe^{3+} to Fe^{2+} at −0.8 V and −0.25 V respectively. Theoretically, iron ($Fe^{3+/2+}$) redox couple arises at 0.77 V with respect to the standard hydrogen reference electrode which corresponds to ~0.86 V vs Hg/HgO. The integral area under all CV curves shows the higher charge storage ability of all the electrodes. It should be noted that the integrated area under the CV curve of bare carbon paper electrodes is much lower than that of deposited electrodes, revealing the negligible contribution of substrate capacitance in total specific capacitance. The CV area of AFO-400 is significantly larger than the other three samples showing its superior performance as a pseudocapacitor electrode. The specific capacity Cs (F g^{-1}) from cyclic voltammetry can be calculated by the following equation:

$$C_s(F\ g^{-1}) = \frac{\int I(V)dV}{2mv\Delta V} \dots\dots (3.2)$$

Where I (A) is the current response, m(g) is the mass of active material, υ (V s^{-1}) is the scan rate and ΔV (V) is the potential window. The excellent capacitive performance of silver ferrite electrodes is also verified from galvanostatic charge-discharge (GCD) experiment within potential ranging from 0.1 to −0.9 V. A longer discharge time corresponds to a high capacitance value due to enhanced effective surface area required for ion adsorption. Figure 3.7b shows the GCD plot of all synthesized samples at 0.8 A g^{-1} current density. From the plot, (Fig. 3.7b) the synthesized electrodes exhibit non-linear charge-discharge behavior with negligible voltage drop, which is distinct from carbon-based material (inverted V shape), denoting the battery along with the EDLC nature of the $AgFeO_2$ electrode. Further, the GCD plot can be divided into three parts, taking the example of discharge one the potential region from 0.1 to −0.7 V have a large slope whereas the −0.7 to −0.9 V region has a small slope, indicating that charge storage comes from preliminary from a double layer produced by

adsorption of electrolyte ions at electrode/electrolyte interface and the low part of the curve (−0.7 to −0.9 V) is mainly due to the reversible reaction of Fe^{2+} to Fe^{3+} ions. The specific capacitance (Cs) of different $AgFeO_2$ samples can be estimated by the following equation:

$$C_s(F\ g^{-1}) = \frac{I\ t_d}{m\Delta V} \ldots\ldots (3.3)$$

Where I (A) is the discharge current, td (s) is the discharge time, m (g) is the mass of active material and ΔV (V) is the potential window. The GCD studies are very well consistent with CV results and specific capacity calculated from CV and charge-discharge profile under different calcination conditions are listed in Table 3.3.

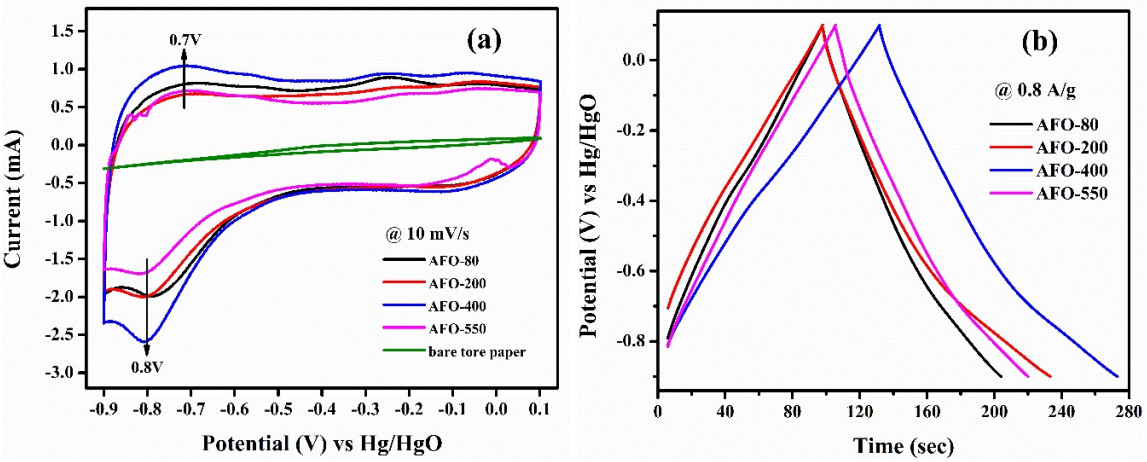

Figure 3.7: Represents (a) CV at 10 mV/s scan rate, and (b) GCD at 0.8 A/g current density, AFO-80, AFO-200, AFO-400, and AFO-550.

Table 3.3: Represents variation in specific capacitance of AFO-80, AFO-200, AFO-400, and AFO-550 calculated from CV and GCD plots.

	AFO-80	AFO-200	AFO-400	AFO-550
C_s(F/g) from CV (10 mV/s)	79.35	74.79	92.47	66.03
C_s(F/g) from GCD (0.8 A/g)	105.9	135.1	141.3	114.3

It is concluded that AFO-400 exhibits superior performance among all synthesized samples. The potential application of AFO-400 as a supercapacitor electrode has further been studied

by carrying out CV experiments at various scan rates depicted in Fig. 3.8a. It may be noticed that the overall specific capacitance decreases as the scan rate increases which could be due to the limited insertion of ions into the pores of the electrode at a short period [as inset of Fig. 3.8a]. The minor shift of redox peak position on increasing the scan rate is due to the polarization effect, while the CV curve maintains its original shape, indicating its utility as a supercapacitor electrode. Further, we have examined the variation of the specific capacitance of AFO-400 as a function of constant current densities shown in Fig. 3.8b. The specific capacitance obtained at different constant current densities of 0.4, 0.8, 1.2, 1.6, and 2 A g^{-1} is 332.9, 141.3, 86.6, 61.4 and 46.9 F g^{-1} respectively [as inset of Fig. 3.8b]. At lower current density ions have enough time to penetrate the inner part of electrode material, while at higher current density an effective utilization of the electrode is limited only to the outer surface of electrodes. As a consequence, capacity decay is observed.

Further, the amount of charge stored in the inner and outer surface of the AFO-400 is quantified using the Power law [150] and the Trasatti plot [160]. It is well known that there are three different mechanisms involved in charge storage such as: (i) faradaic reaction through intercalation/de-intercalation of ions, (ii) faradaic reaction through surface redox reaction, and (iii) electric double layer (EDLC) formation at the electrode/electrolyte interface. According to Power's law, the scan rate-dependent CV current can be expressed as:

$$i = a\upsilon^{b} \ldots\ldots (3.4)$$

$$\log i = \log a + b \log \upsilon \ldots\ldots (3.5)$$

where, a and b are the adjustable parameters, and υ is the scan rate (V/s), The b value can be obtained from the slope of log(i) vs log(υ) at the peak potential (−0.75 V) shown in Fig. 3.8c. Theoretically if the b-value is 0.5, CV current obeys the intercalation/de-intercalation mechanism, and if the b-value is 1, the CV current corresponds to a capacitive mechanism. In the present case, b lies between 0.7 to 0.9, suggesting CV current is the combination of both capacitive and EDLC.

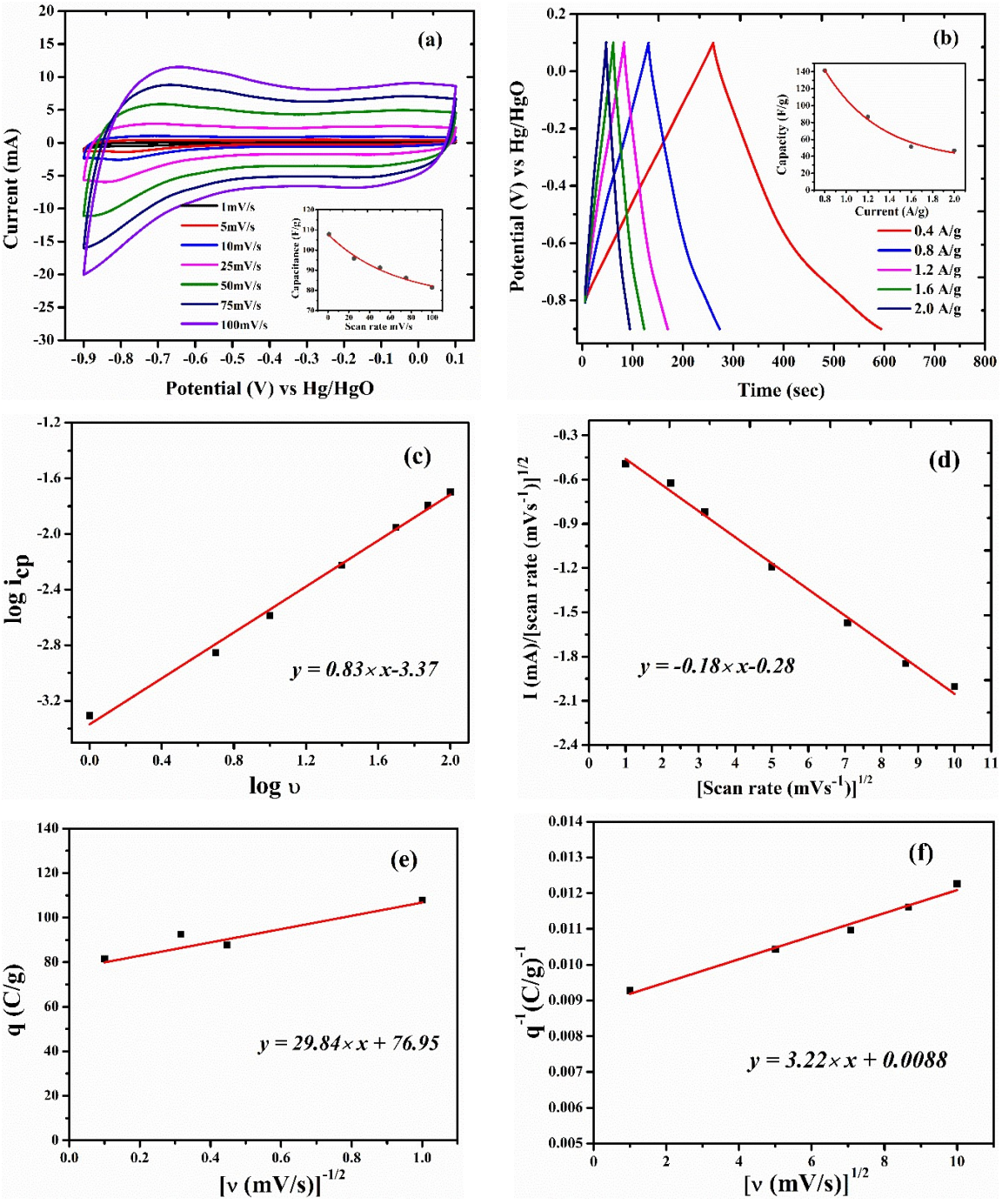

Figure 3.8: (a) CV at different scan rates starting from 1mV/s to 100 mV/s inset show variation in specific capacitance with scan rates, (b) GCD at different current densities from 0.4A/g to 2A/g of AFO-400 inset show variation in specific capacitance with current densities, (c) plot between log i_{cp} vs log υ, (d) plot between i/ $υ^{1/2}$ vs $υ^{1/2}$ at cathodic peak potential and (e, f) corresponds to the Trasatti plot.

So, at the fixed potential the capacitive and intercalation current can be quantified using the following equation:

$$i(V) = k_1\upsilon + k_2\upsilon^{\frac{1}{2}} \ldots\ldots (3.6)$$

This can be modified into

$$\frac{i(V)}{\upsilon^{1/2}} = k_1\upsilon^{1/2} + k_2 \ldots\ldots (3.7)$$

where, $k_1\upsilon$ and $k_2\upsilon^{1/2}$ represent the current contribution from capacitive and intercalation of ions, respectively. The value of k_1 and k_2 can be obtained from the slope and intercept of the plot between $i(V)/\upsilon^{1/2}$ and $\upsilon^{1/2}$ shown in Fig. 3.8d. We have further quantified charge stored at the inner and outer surface of the electrode using Trasatti plot. Figures 3.8e and 3.8f show the Trasatti plot of AFO-400 electrodes. The y-intercept of the linear fit of q^{-1} vs $\upsilon^{1/2}$ at υ = 0 represents the total amount of charge stored in the inner structure of the electrode Fig. 3.8f, on the other hand, the y-intercept of the linear fit of q vs $\upsilon^{-1/2}$ at υ = 0 a show the amount of charge stored at the outer surface of the electrode Fig. 3.8e. So, the charge storage contribution from the inner electrode is calculated as $Q_{total} - Q_{out}$. According to Trasatti's plot Q_{out} and Q_{in} are found to be 77 and 35 C g^{-1} respectively.

In the CV of Fig. 3.9a, the pink shaded area shows the diffusion contribution while the blue shaded area shows the capacitive contribution of AFO-400 at 10 mV s^{-1} scan rate. Fig. 3.9b shows the histogram of intercalation and capacitive contribution at various scan rates, at a low scan rate, the total current is the combination of both intercalation and EDLC, while at a high scan rate, the intercalation current is negligible. Overall, it can be concluded that the capacitive mechanism is the dominant over redox in AFO-400 and the open channel structure facilitates the charge storage mechanism.

Furthermore, it is important to elucidate the cyclic performance of electrode material for its practical application as a supercapacitor electrode. The cyclic stability of AFO-400 is tested up to the 2000^{th} cycle by applying continuous charge/discharge constant current density of 2 A g^{-1} as illustrated in Fig. 3.9c.

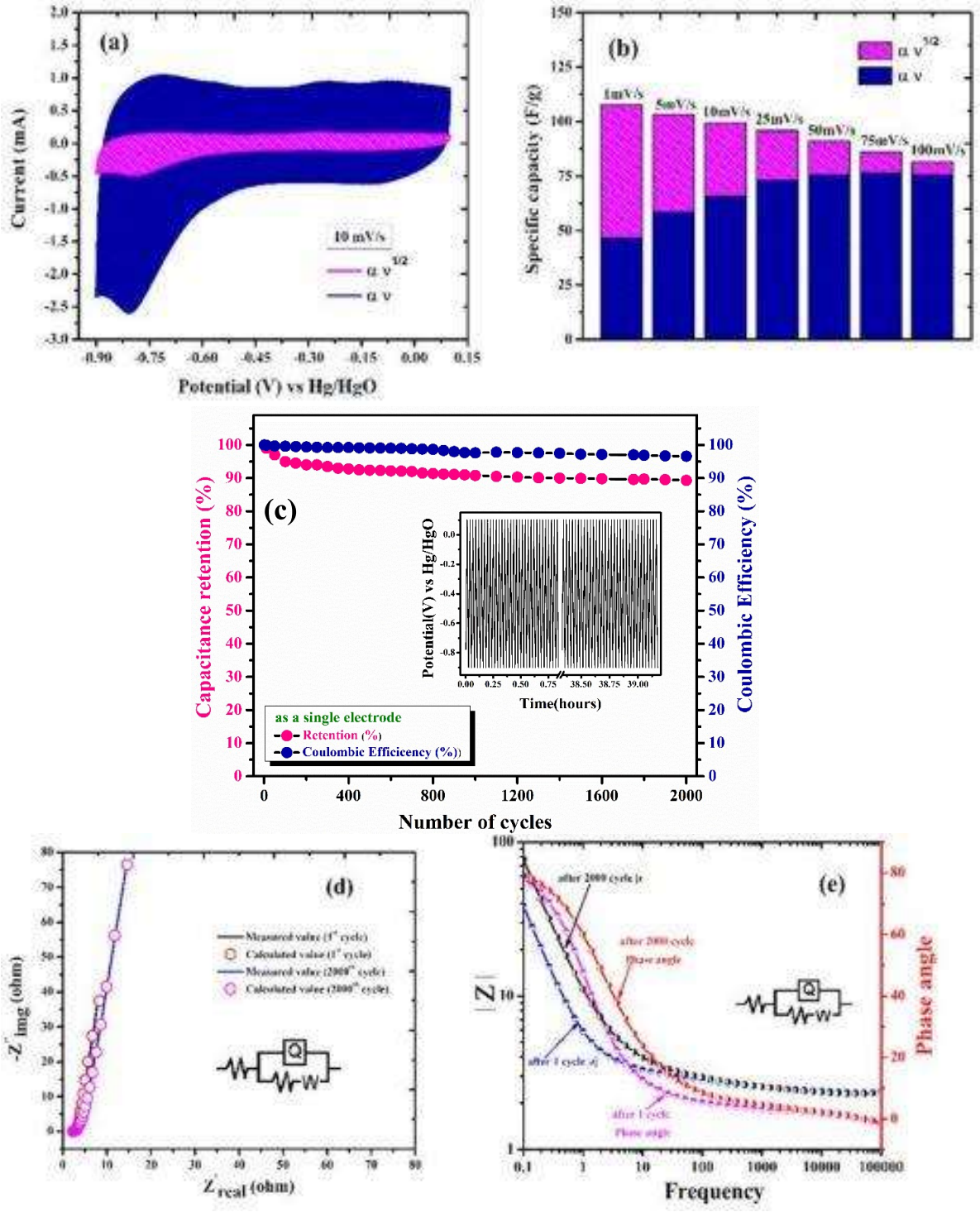

Figure 3.9: : (a) CV of intercalation and surface contribution at 10 mV/s, (b) variation of specific capacity (intercalation vs surface capacitance) at different scan rate, (c) cyclic stability of AFO-400, (d) & (e) represent Nyquist and bode plot of AFO-400 after 1st and 2000th cycle.

We have further studied the kinetic parameters of synthesized silver ferrites by using electrochemical impedance spectroscopy (EIS) in the frequency range of 10 kHz to 0.1 Hz in 1 M Na_2SO_4 electrolyte at room temperature. In the Nyquist plot, the intercept made at the x-axis at high-frequency region represents series resistance (R_s), a small semicircular arc shows charge transfer resistance (R_{ct}) along with double layer capacitance (C_{dl}), while a straight line-making angle with the x-axis at lower frequency range corresponds to diffusion path of ions. Nyquist plots of all electrodes exhibit a similar type of distorted semicircle with a straight line. The R_{ct} values of all electrodes are approximately equal. The less sloppy nature of the curve of AFO-80 and AFO-200 indicates a smaller number of grains compared to the AFO-400 sample. AFO-550 possesses a straight vertical line due to significant changes in the structure of the electrode. Figures 3.9d and 3.9e show the Nquist and Bode plot (the inset shows the corresponding equivalent circuit) of AFO 400. The excellent electrochemical performance of the AFO-400 electrode is due to the combined effect of surface charge storage and diffusion of ions. In brief, the optimized concentration of the 2H phase in AFO-400 provides superior Na^+ ion adsorption and diffusion at the electrode, as a result, 89% of capacity retention is observed after the 2000^{th} cycle shown in Fig. 3.9c.

3.3.6 Electrochemical study of Symmetrical and Asymmetrical Cell

In order to demonstrate the practical application of $AgFeO_2$ in energy storage devices the symmetrical and asymmetric cell in which AFO-400 as negative electrode and activated carbon as positive electrode are fabricated and tested in 1 M Na_2SO_4 aqueous electrolyte. The specific capacities for SSC and ASC devices (within the potential range from 0 to 1.4 V) can be calculated from the CV plot and found to be ~36 and 48 F g^{-1} at 10 mV s^{-1} while from the GCD curve, the obtained values are ~33 F g^{-1} and 43 F g^{-1} at 1 A g^{-1} current density respectively. It is apparent that the charge and discharge time of the ASC is longer than that of the SSC devices, showing that the specific capacitance of the ASC is higher than that of the SSC devices. From single electrode measurements, it is observed that AFO-400 shows stable electrochemical performance within the voltage range of 0 to −1 V, whereas activated carbon exhibits stable performance in the range of 0 to 1 V against Ag/AgCl reference electrode. Fig. 3.10c depicts individual cyclic voltammetry curves, of AFO-400 and AC at 50 mV s^{-1} scan rate. In order to counterbalance the specific capacitance of as fabricated ASC,

the mass balance has been done using the following equation, and obtained mass ratio of AFO-400 to AC is 0.83.

$$\frac{m_+}{m_-} = \frac{C_-}{C_+}\frac{\Delta V_-}{\Delta V_+} \ldots\ldots (3.8)$$

Fig. 3.10d shows the CV curves for ASC comprising AFO-400//AC for different potential windows at a scan rate of 25 mV s^{-1} in 1 M Na_2SO_4 electrolyte. The fabricated ASC shows an ideal capacitor behavior with a rectangular shape that is consistent up to the 1.8 V potential window. Thus, ASC should exhibit superior performance up to 1.8 V. Fig. 3.10e shows the CV curves of AFO-400//AC (ASC) at scan rates of 1, 5, 10, 25, 50, 75, and 100 mV s^{-1} scan rates between 0 to 1.8 V of operating window in aqueous 1 M Na_2SO_4 electrolyte. The CV profiles retain their rectangular shape and symmetry with increasing potential scan rate, indicating that fabricated ASC exhibits superior capacitor behavior. The maximum specific capacity for ASC is found to be 81.30 F g^{-1} at a scan rate of 1 mV s^{-1}, while on increasing scan rate up to 10 mV s^{-1}, it maintains its capacity up to 58.5 F g^{-1}, which is significantly higher than other recently reported iron oxide based ASC namely, α-Fe_2O_3 NRs//MnO_2 ASC (23 F g^{-1} at scan rate of 10 mV s^{-1}), $MnFe_2O_4$//AC ASC (51.9 F g^{-1} at scan rate of 5 mV s^{-1}) etc. The ASC reported in this study retains its capacitance value of ~38.5 F g^{-1} as the scan rate increases from 1 mV s^{-1} to 100 mV s^{-1}.

Superior electrochemical performance for the ASC is further established by the constant-current charge/discharge method and related data at different current densities are shown in Fig. 3.10f. As can be seen from the data, at higher current densities, the charge/discharge profiles are more symmetrical and linear, indicating ideal-capacitive behavior with fast charge/ discharge characteristics for the ASC. Form the discharge profile, maximum value of specific capacitance is found to be ~75 F g^{-1} at a discharge current density of 0.4 A g^{-1}, which is also significantly higher than the values reported for other iron-oxide-based ASCs, like MnO_2//FeOOH ASC (51 F g^{-1} at load current of 0.5 A g^{-1}), Fe_3O_4//MnO_2 ASC (23 F g^{-1} at load current of 0.27 A/g), $LiMn_2O_4$//$MnFe_2O_4$ ASC (~50 F g^{-1} at load current of 0.5 A g^{-1}), etc.

Table 3.4: Represents the rate capability of AFO-400//AC estimated by cyclic voltammetry and charge-discharge experiments.

AFO-400//AC						
Cyclic voltammetry	Scan rate (mV/s)	10	25	50	75	100
	Specific capacity (F/g)	58.5	47.5	43	40.5	38.5
Charge-discharge	Current density (A/g)	0.4	0.8	1.2	1.6	2
	Specific capacity (F/g)	74.6	34.5	21	15	12

For further understanding of the behavior of the supercapacitor, the impedance of AFO-400//AC is taken after the 1st and 2000th cycle, and results are shown in Fig. 3.10b. The EIS data is analyzed using Nyquist plots. At the high-frequency region both the Nyquist plots show similar types of behavior but at the low-frequency region, the slope of both curves is different. A nearly vertical line at a low-frequency region demonstrates ideal capacitive behavior while a slope of 45° corresponds to semi-infinite diffusion/transport of ions in the electrolyte. After the 2000th cycle, the less sloppy nature of the curve is probably due to the accumulation of ions into the pores of the electrode, and the loss of capacitance is due to the decrease of electrolyte ions and electrical contact between the active material and the substrate. The cyclic stability of the fabricated ASC device is tested up to the 2000th cycle by applying continuous charge/discharge constant current density of 2 A g^{-1} as shown in Fig. 3.10a.

The power density (P) and energy density (E) are the important parameters for illustrating the electrochemical performance of ASC and can be calculated using the following equation:

$$E\left(\frac{Wh}{kg}\right) = \frac{0.5 \times C_{ASC} \times \Delta V^2}{3.6} \ldots\ldots (3.9)$$

$$P\left(\frac{W}{kg}\right) = \frac{E \times 3600}{t_{dis}} \ldots\ldots (3.10)$$

The maximum energy density that has been achieved for the ASC is 33.8 Wh kg^{-1} at a load-current density of 0.4 A g^{-1} with a corresponding power density of 454.3 W kg^{-1}. The energy density is found to be 5.3 Wh kg^{-1} with a maximum power density of 498.5 W kg^{-1} when

the load current density is increased by 5 times, representing an excellent rate performance for the ASC. These values are more promising than other recently reported iron oxide-based electrode material with a cell voltage of 1.8 V, namely, 7 Wh kg^{-1} and 820 W kg^{-1} for Fe_3O_4//MnO_2 ASC, 12 Wh kg^{-1} and 3700 W kg^{-1} for FeOOH//MnO_2 ASC, 7.86 Wh kg^{-1} and 1918.5 W kg^{-1} for α-Fe_2O_3-NRs//MnO_2–ASC, 10.25 Wh kg^{-1} and 3076 W kg^{-1} for $MnFe_2O_4$//AC ASC, 32.5 Wh kg^{-1} and 1.6 kW kg^{-1} for MnO_2 nanowires//α-Fe_2O_3 nanotube ASC. Overall, the good performance of the AFO-400//AC device is observed that can be applied for supercapacitor application.

3.4 Conclusions

In summary, for the first time, the silver-iron containing delafossites having layered structure was explored as a pseudocapacitor electrode. A series of $AgFeO_2$, mixing with 2H (hexagonal) and 3R (rhombohedral) phases were successfully synthesized via a simple co-precipitation route at different calcination temperatures (80 °C, 200 °C, 400 °C and 550 °C). This study demonstrated that calcination treatment played a crucial role in the phase tuning of the 2H phase in the $AgFeO_2$ crystal. The specific capacitance of $AgFeO_2$ calcined at 400 °C had the majority of 2H-phase, exhibiting the best capacitive performance (110.4 F g^{-1} at 1 A g^{-1} current density) with 89% capacity retention after the 2000^{th} cycle. This improvement in capacitance was attributed due to the larger inter-layer spacing of the 2H phase, which resulted in better accessibility of Na^+ ions into the internal structure of electrodes. Additionally, the flower-like microarchitecture provided an easy diffusion path for charge transfer of Na_2SO_4 electrolyte over entire the sample range. Furthermore, an asymmetric device was fabricated by coupling with AFO-400 as negative and activated carbon as positive electrode and using a cellulose separator soaked in 1 M Na_2SO_4 electrolyte. Maximum energy and power density values that had been achieved for ASC were ~33.6 Wh kg^{-1} and ~454 W kg^{-1}, respectively. The ASC exhibits compelling cycling stability with more than 86% capacitance retention over 2000^{th} cycles. These findings suggested that a silver-iron-based layered structure could be a promising anode electrode for electrochemical pseudocapacitor applications.

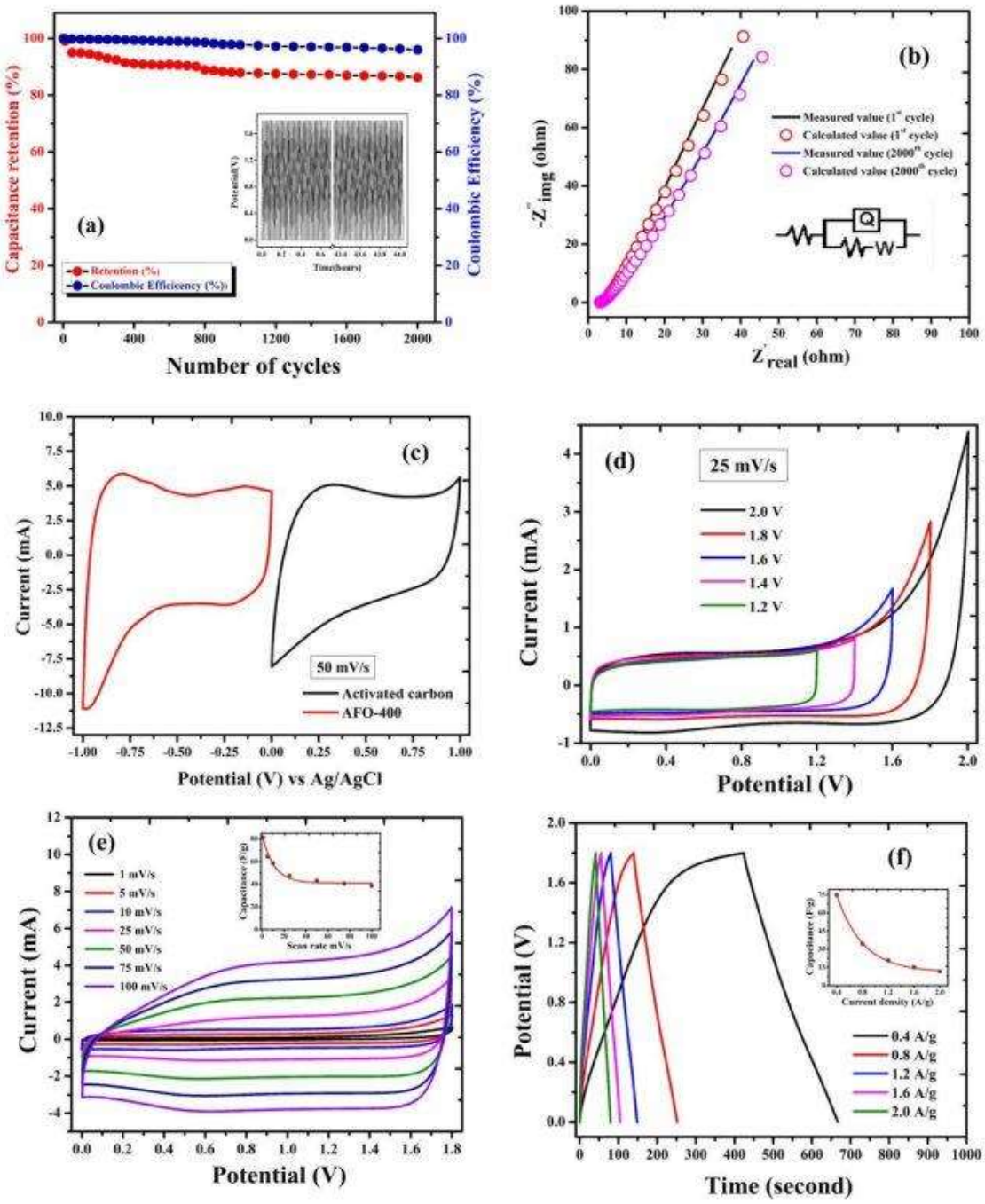

Figure 3.10: (a) Cyclic test of ASC cell at 2 A/g current density during 2000th cycles, (b) Nyquist plot of ASC cell after 1st and 2000th cycles (c) individual CV curves of AFO-400 and AC electrode in three-electrode cell at 50 mV/s scan rate, (d) CV of AFO-400//AC ASC cell recorded within different operational potential window, (e) CV curves of AFO-400//AC recorded as a function of scan rates, and (f) Charge/discharge profile at different current densities.